Journal of Computational Physics **153,** 312–333 (1999)
Article ID jcph.1999.6279, available online at http://www.idealibrary.com on IDEAL®

High-Order Compact-Difference Schemes for Time-Dependent Maxwell Equations

J. S. Shang

Air Vehicles Directorate, Air Force Research Laboratory, Wright–Patterson AFB, Ohio 45433-7913

Received May 21, 1998; revised December 21, 1998

Two high-order compact-difference schemes have been developed for solving three-dimensional, time-dependent Maxwell equations. Spurious high-frequency oscillatory components of the numerical solution, which are considered to be among the principal sources of time instability, are effectively suppressed by a spatial filter. The present numerical schemes are validated by calculations of three-dimensional transient electromagnetic waves within a waveguide, an oscillating electric dipole, and the radar cross section of perfectly electrical conducting sphere.

1. INTRODUCTION

Time-dependent Maxwell equations have been established for over 125 years as the theoretical representation of electromagnetic phenomena [1]. However, the accuracy requirement of high-frequency or transient simulations is severe both in dynamic range and in absolute value [2, 3]. Practical applications of computational electromagnetics in the time domain are limited mostly to the resonance regime. Improved numerical efficiency becomes a pacing item for expanding the application envelope of computational electromagnetics in the time domain. For multi-dimensional calculations, the truncation error of a numerical result is manifested in dissipative, dispersive, and anisotropic errors. The accumulated numerical error during a sustained period of calculations or in an extensive computational domain may lead to a situation where the wave modulation and phase errors become unacceptable.

Numerical resolution is naturally quantifiable by Fourier analysis in terms of normalized wavenumber. In applications, the quantification is measured by the grid-point density per wavelength. Thus a direct correlation between the grid-point density and the wavenumber exists. All numerical schemes have a limited wavenumber range for accurate computations. For most popular second-order accurate numerical methods using an unstaggered mesh system, the rule of thumb for acceptable accuracy is at least 20 nodes per wavelength [2, 3]. However, this simple grid density criterion becomes insufficient when the computational

0021-9991/99

domain contains multiple media with a wide range of characteristic impedances. At present, for a high-frequency CEM simulation or a large electrical configuration, the number of mesh points needed to meet an accuracy specification is often beyond the reach of conventional computing systems. The need to develop high-resolution schemes for extending the present CEM simulation capability to high-frequency spectra is urgent.

Using the formal order of accuracy of truncation errors exclusively to select an algorithm for time-dependent simulation is an oversimplification [4–9]. According to Tam [6] and Lele [4], the desired feature of a numerical scheme may be derived from optimization in the Fourier space rather than by focusing on the lowest possible truncation error. In light of this line of reasoning, compact differencing and optimized finite differencing are viable methods by which to achieve high resolution. Both approaches seek algorithms that have a small stencil dimension and yet maintain a lower level of dispersive and dissipative error than conventional numerical schemes. Collatz [7] has pointed out that the compact difference scheme is based on Hermite's generalization of the Taylor series. The basic formulation is an implicit procedure for evaluating the derivatives of the dependent variables. The stencil structure for most compact-difference formulas is spatially central and requires additional derivative values at boundaries [4, 5, 7–10]. The spatially central scheme is inapplicable to the immediately adjacent grid point of a boundary for stencil dimensions greater than three. An additional transitional scheme from the boundary to interior domain is required. This transitional boundary scheme not only is required to transmit data from the boundary but also must preserve the stability and accuracy of interior domain for the global order or resolution. These unique features of compact-difference schemes are also the sources of spurious high-frequency numerical oscillations. For this reason, the development of a numerical boundary scheme is emerging as a major difficulty associated with high-resolution methods [9–14].

An undesirable feature of compact-difference schemes is the time instability during a long-time integration process [5, 11–13]. There are some exceptions, such as the Turkel's scheme when applied to a two-dimensional staggered mesh [2] or when the periodicity boundary condition is applicable [4]. Although these high-order schemes are stable in the classical sense [15–19], numerical results frequently exhibit a nonphysical growth in time. Efforts by Carpenter, Gottlieb, and Abarbanel [5, 19] have shown that even satisfying the generalized summation-by-parts energy norm formulation [16] is not sufficient for preventing time instability. Time instability is incurred by a positive real eigenvalue component of a spatial operator matrix. This eigenvalue will dominate the numerical results after a long-time evolution (5). A possible remedy is to provide specific boundary treatment, by introducing the simultaneous approximation term (SAT) to scalar equations [4]. Another option is to utilize a low-pass filter that eliminates the destabilizing Fourier components from the numerical results [11, 20]. The latter approach will be pursued in the present analysis.

Compact-differencing-based finite-volume procedures developed to solve Maxwell equations [11–13] recently have been applied successfully to Navier–Stokes equations in finite-difference form [14]. Gaitonde and Shang [11, 12] and Visbal and Gaitonde [14] have devised a staged compact-difference approach, including a spatial filter, to transmit data from the boundary to the interior computational domain. The boundary scheme with a narrow stencil must not be more than one order of accuracy lower than the interior scheme to bridge the stencil limit [17]. On the boundary, the derivative data required by the compact formulation is generated by a one-sided difference approximation [9, 11–12]. The spurious high-frequency numerical oscillations induced either by the numerical procedure or by

mesh stretching are then suppressed by a spatial filter. The numerical behavior of the spatial filter has been carefully studied by Fourier analysis [20, 21] and proven to be effective in suppressing numerical instability.

In the present analysis, the compact-difference procedure [4, 11–14] is implemented for a finite-difference approximation to solve the time-dependent Maxwell equations. Research emphasis is placed on the important aspect of boundary condition implementation. It is hoped that additional salient features of the compact-difference approximation to the time-dependent Maxwell equations will emerge. For the present analysis, a fourth-order Runge–Kutta method [22] is adopted for integration with respect to time. A fourth- and a sixth-order compact-difference approximation, incorporated with suitable spatial filters, are developed to simulate a three-dimensional oscillating electric dipole, transient electromagnetic waves within a rectangular waveguide, and the radar cross section (RCS) of a perfectly electrical conducting (PEC) sphere.

2. GOVERNING EQUATIONS

The time-dependent Maxwell equations for an electromagnetic field in free space can be given as [1]

$$\frac{\partial B}{\partial t} + \nabla \times E = 0 \tag{1}$$

$$\frac{\partial D}{\partial t} - \nabla \times H = 0 \tag{2}$$

$$\nabla \cdot B = 0, \qquad B = \mu H \tag{3}$$

$$\nabla \cdot D = 0, \qquad D = \epsilon E, \tag{4}$$

where ϵ and μ are the electric permittivity and the magnetic permeability which relate the electric displacement to the electric field intensity and magnetic flux density to the magnetic field intensity, respectively.

The time-dependent Maxwell equations can be cast in flux-vector form on a general curvilinear and body conformal frame of reference by a coordinate transformation from the Cartesian system. The governing equations become [23, 24]

$$\frac{\partial U}{\partial t} + \frac{\partial F_\xi}{\partial \xi} + \frac{\partial F_\eta}{\partial \eta} + \frac{\partial F_\zeta}{\partial \zeta} = 0, \tag{5}$$

where U is the transformed dependent variable. The dependent variable U is scaled by the reciprocal of the Jacobian of the coordinate transformation, J,

$$U = \{B_x/J,\, B_y/J,\, B_z/J,\, D_x/J,\, D_y/J,\, D_z/J\}^T. \tag{6}$$

F_ξ, F_η, and F_ζ and the contravariant components of the flux vectors on the Cartesian coordinates. They are presented as

$$\begin{aligned} F_\xi = [&(-\xi_z D_y + \xi_y D_z)/\epsilon,\ (\xi_z D_x - \xi_x D_z)/\epsilon,\ (-\xi_y D_x + \xi_x D_y)/\epsilon, \\ &(\xi_z B_y - \xi_y B_z)/\mu,\ (-\xi_z B_x + \xi_x B_z)/\mu,\ (\xi_y B_x - \xi_x B_y)/\mu]/J \end{aligned} \tag{7}$$

$$F_\eta = [(-\eta_z D_y + \eta_y D_z)/\epsilon,\ (\eta_z D_x - \eta_x D_z)/\epsilon,\ (-\eta_y D_x + \eta_x D_y)/\epsilon,$$
$$(\eta_z B_y - \eta_y B_z)/\mu,\ (-\eta_z B_x + \eta_x B_z)/\mu,\ (\eta_y B_x - \eta_x B_y)/\mu]/J \tag{8}$$
$$F_\zeta = [(-\zeta_z D_y + \zeta_y D_z)/\epsilon,\ (\zeta_z D_x - \zeta_x D_z)/\epsilon,\ (-\zeta_y D_x + \zeta_x D_y)/\epsilon,$$
$$(\zeta_z B_y - \zeta_y B_z)/\mu,\ (-\zeta_z B_x + \zeta_x B_z)/\mu,\ (\zeta_y B_x - \zeta_x B_y)/\mu]/J. \tag{9}$$

3. INITIAL CONDITIONS AND BOUNDARY VALUES

The transverse electrical wave propagation within a waveguide, the oscillating electric dipole, and the scattering phenomenon share common boundary conditions on the interface of different media. Since the sphere and the waveguide are assumed to have perfect electrical conductivity, the appropriate boundary conditions at the surfaces are [1]

$$\begin{aligned} \vec{n} \times (E_1 - E_2) &= 0 \\ \vec{n} \times (H_1 - H_2) &= J_s \\ \vec{n} \cdot (B_1 - B_2) &= 0 \\ \vec{n} \cdot (D_1 - D_2) &= \rho_s. \end{aligned} \tag{10}$$

The above requirements imply that the normal component of the total magnetic field is zero on the conductor surface [1]. Thus, the electromagnetic field is discontinuous at the interface of two media. Following previous efforts [23, 24], the unknown surface current and charge densities, J_s and ρ_s, are treated as finite jumps of constant value. Two extrapolated numerical boundary conditions for the finite jump of properties at the surface are introduced to replace the equations that contain unknowns. This formulation is compatible with the basic attribute of the hyperbolic partial differential system, which allows piecewise continuous data to propagate unaltered along a characteristic.

The advantage of the flux-vector formulation is also revealed in the implementation of the farfield boundary condition. If one of the coordinates is aligned with the direction of wave motion, the compatibility condition at the truncated boundary is satisfied identically [23, 24]. For the oscillating electrical dipole problem and the transient electromagnetic wave in a waveguide, the farfield and the boundary condition at the exit plane are numerically exact. The farfield boundary conditions are specified simply by assigning the flux-vector component aligned with the negative eigenvalue to zero, $F^- = 0$ [23, 24]. The compatibility conditions for the oscillating electrical dipole can be derived from the null space vectors given as

$$\begin{aligned} \sqrt{\mu/\epsilon\left(\xi_x^2 + \xi_y^2 + \xi_z^2\right)}(\xi_y B_x - \xi_x B_y) + D_z &= 0 \\ \sqrt{\mu/\epsilon\left(\xi_x^2 + \xi_y^2 + \xi_z^2\right)}\left[-\left(\xi_x^2 + \xi_z^2\right)B_x - \xi_x \xi_z B_y\right] + \xi_z D_y &= 0 \\ \sqrt{\mu/\epsilon\left(\xi_x^2 + \xi_y^2 + \xi_z^2\right)}\left[\left(\xi_x \xi_y B_x + \left(\xi_y^2 + \xi_z^2\right)B_y\right] + \xi_z D_x &= 0 \\ \xi_x B_x + \xi_y B_y + \xi_z B_z &= 0. \end{aligned} \tag{11}$$

For the transient electromagnetic wave in the rectangular waveguide, these boundary conditions can be developed further in terms of phase velocity. Since the rank of a flux-vector matrix degenerates from a general curvilinear coordinate to the Cartesian system, only two

linearly independent relationships exist. The boundary condition of the transverse electrical wave at the exit plane of the waveguide becomes

$$\begin{aligned} \omega B_x + \sqrt{\omega^2\mu\epsilon - [(n\pi/a)^2 + (m\pi/b)^2]}Dy = 0 \\ \omega B_y - \sqrt{\omega^2\mu\epsilon - [(n\pi/a)^2 + (m\pi/b)^2]}D_x = 0, \end{aligned} \tag{12}$$

where a and b are the cross-sectional physical dimensions of the rectangular waveguide and ω is the angular frequency of the transverse electric wave.

For the scattering sphere problem, at the truncated farfield boundary, the vanishing incoming flux component reduces to an effective approximation [23, 24]. In the scattered-field formulation, the placement of the farfield is aided by the coordinate stretching technique. By using a geometric progression series with a constant $k = 1.05$, $\Delta r_n = k^{n-1}\Delta r_0$, the farfield boundary can be moved several wavelengths away with just a few additional grid points. This boundary condition may be inferior in accuracy to the perfect matched layer approach by Berenger [25–27], but no additional equations are required to be solved.

The incident wave of scattering simulation consists of a linearly polarized harmonic field propagating in the negative z-axis direction, whose components are given by

$$\begin{aligned} B_y &= -A\sqrt{\epsilon\mu}\sin(\omega t + kz) \\ D_x &= A\epsilon\sin(\omega t + kz), \end{aligned} \tag{13}$$

where A denotes the amplitude of the incident wave. For the present investigation, a value of unity is assigned. Initially, the incident field is specified over the entire computational domain. This initial condition is preferred over the prescription of a completely quiescent computational domain to reduce the transient period of incident excitation.

4. TEMPORAL AND SPATIAL DISCRETIZATION

The present approach uses Runge–Kutta schemes for time integration. This first-order derivative evaluation procedure can be fitted into a Taylor series by the constraint of weighting coefficients that retain a prescribed order of accuracy [22]. The adopted four-stage method can be expressed as

$$\begin{aligned} U^{n+1} &= U^n + (\Delta t/6)\cdot(U_1' + 2U_2' + 2U_3' + U_4') \\ U_1' &= U_1'(t, U^n) \\ U_2' &= U_2'\big(t + \Delta t/2, U^n + \Delta t/2 \cdot U_1'\big) \\ U_3' &= U_3'\big(t + \Delta t/2, U^n + \Delta t/2 \cdot U_2'\big) \\ U_4' &= U_4'\big(t + \Delta t, U^n + \Delta t \cdot U_3'\big). \end{aligned} \tag{14}$$

Spatial derivatives are evaluated by compact-difference schemes. In short, the numerical procedure is implicit in the derivative evaluation and requires additional data at the boundary. The most general compact difference, or the Hermitian formula, can be written to include first- and second-order derivatives [4, 7]. For CEM in the time domain, the formula containing only the first derivatives is sufficient:

$$\alpha U_{i-1}' + U_i' + \alpha U_{i+1}' = C_2(U_{i+2} - U_{i-2}) + C_1(U_{i+1} - U_{i-1}). \tag{15}$$

The present fourth- and sixth-order formulations are subsets of a system developed by Lele [4]. The coefficients and a parameter of the formulation are interrelated as

$$\begin{aligned} C_2 &= (4\alpha - 1)/3 \\ C_1 &= 2(\alpha + 2)/3. \end{aligned} \tag{16}$$

By selecting $\alpha = \frac{1}{4}$, the stencil of this formulation degenerates into a three-point scheme, the well-known Pade formula [4, 7]. A sixth-order scheme is recovered by assigning $\alpha = \frac{1}{3}$ and the formulation requires a five-point stencil. From a Fourier analysis of the one-dimensional model wave equation, both the fourth- and sixth-order schemes are conditionally stable. The fourth- and sixth-order schemes have allowable Courant–Friederichs–Levy (CFL) numbers of 1.63 and 1.42, respectively.

Numerical stability is a critical concern for compact-difference methods, which must include a stable boundary scheme to preserve the global accuracy [5, 9, 11–14]. Nearly all compact-difference schemes are spatially central, except perhaps the Adam third-order method [8], which has a bidiagonal structure. Nevertheless, the values of derivatives at the boundary must be provided. Usually this numerical boundary value is obtained by a one-sided difference approximation. This process is performed repeatedly for each temporal step to update time-dependent computations. For the sixth-order or higher shceme, the stencil dimension involves five points or more and a boundary scheme becomes necessary. The basic idea of using the staged one-order-lower approximation for the boundary scheme is derived from the summation-by-parts energy mode analysis [17–19]. For a hyperbolic system, this constraint is explicit [17, 18]. Therefore, a formally sixth-order interior scheme must be supported by a fifth-order boundary scheme. In most practical applications, this procedure is the source of numerical instability manifested by spurious high-frequency oscillations. A fourth-order and a fifth-order explict one-sided difference formula are given as

$$\begin{aligned} U_i' &= (-25U_i + 48U_{i+1} - 36U_{i+2} + 12U_{i+3} - 3U_{i+4})/12\Delta\xi \\ U_i' &= (25U_i - 48U_{i-1} + 36U_{i-2} - 12U_{i-3} + 3U_{i-4})/12\Delta\xi \end{aligned} \tag{17}$$

$$\begin{aligned} U_i' &= (-137U_i + 300U_{i+1} - 300U_{i+2} + 200U_{i+3} - 75U_{i+4} + 12U_{i+5})/60\Delta\xi \\ U_i' &= (137U_i - 300U_{i-1} + 300U_{i-2} - 200U_{i-3} + 75U_{i-4} - 12U_{i-5})/60\Delta\xi. \end{aligned} \tag{18}$$

Assessments of the formal order of accuracy for the staged approximation for multidimensional calculations are extremely difficult. Some interesting results on uniform and curvilinear grid systems can be found in Refs. [11–14].

5. LOW-PASS SPATIAL FILTER

In principle, time instability, which occurs in solving the hyperbolic systems, can be eliminated by an SAT in treating the boundary conditions [5]. For a scalar equation, this procedure has demonstrated the ability to eliminate the numerical instability while maintaining the formal oder of accurracy for the numerical method. However, the generalization to treat a system of equations has not yet been accomplished. For this reason, an alternative approach is adopted in the present effort to suppress the time instability.

The numerical instability of compact-difference schemes is usually manifested in the form of spurious high-frequency Fourier components of the numerical solution [5, 11–14, 19]. An effective remedy can be derived by modifying only the amplitude of Fourier components within a restricted frequency spectrum [20]. This mechanism is realizable by a filter, which can be implemented in time or in space. However, in the temporal approach, a data window in time must be maintained, which will require additional computing resources. In contrast, the spatial filter does not incur this additional expenditure and is more attractive for applications. From ealier efforts in developing compact-difference schemes [11, 13], the higher frequency modes of solutions always become unstable first. Therefore, the numerical stability should be enhanced by modifying or suppressing the amplitude of high-frequency components. Equally important, these components are already unsupportable by the grid system and are considered to be parasitic.

A low-pass filter [20, 21] is ideal for the elimination of undesirable high-frequency Fourier components and does not affect the remaining components of a numerical solution. In addition, the adopted spatial filter modifies only the amplitude but not the phase relationship among all Fourier components of the solution. The spectral function of a symmetric numerical filter contains no imaginary part and has the ideal low-pass amplitude response [20]. A tridiagonal filter can be given as [11–13]

$$\beta U_{i-1} + U_i + \beta U_{i+1} = \Sigma a_n (u_{i+n} + u_{i-n})/2, \qquad n = 0, 1, 2, \ldots, N, \tag{19}$$

where the variables U and u represent the filtered and raw values, respectively. The only free parameter of the spatial filter is bounded by the values $-0.5 < \beta < 0.5$. It is interesting to note that when the parameter β is assigned a value of zero, the filter becomes an explicit operator. The filter degenerates to an identity, i.e., the computed results will not be modified, when the value of β approaches 0.5. The coefficients of the symmetric filter can be obtained by expanding and matching the spectral function, $\mathrm{SF}(\omega) = \Sigma a_n \cos(n\omega)/[1 + 2\beta \cos(\omega)]$, in a Maclaurin series. The coefficients for a fourth-, sixth-, and eighth-order filter are included in Table 1. The detailed analysis of the frequency response of this spatial filter, including the coefficient matching, can be found in Ref. [12].

In Fig. 1, the numerical behavior of the two selected spatial filters is depicted over the entire normalized wavenumber $(2\pi\kappa\Delta x/L)$ range, π. It is immediately recognizable that the frequency responses of the sixth- and eighth-order filters suppress only the amplitude of the highest frequency components. The effectiveness of the parameter β in regulating the filter behavior is also clearly exhibited. For the eighth-order filter, the amplitude of Fourier components with a wavenumber higher than $\frac{\pi}{4}$ will be gradually suppressed. This threshold

TABLE 1
Coefficients of Spatial Filter Formula

Coefficient	Fourth order	Sixth order	Eighth order
a_0	$\frac{3(2\beta-1)}{8} + 1$	$\frac{5(2\beta-1)}{16} + 1$	$\frac{35(2\beta-1)}{128} + 1$
a_1	$\frac{(2\beta-1)}{2} + 1$	$\frac{17(2\beta-1)}{32} + 1$	$\frac{9(2\beta-1)}{16} + 1$
a_2	$\frac{(2\beta-1)}{8}$	$\frac{3(2\beta-1)}{16}$	$\frac{7(2\beta-1)}{32}$
a_3	0	$\frac{-(2\beta-1)}{32}$	$\frac{-2(2\beta-1)}{32}$
a_4	0	0	$\frac{(2\beta-1)}{128}$

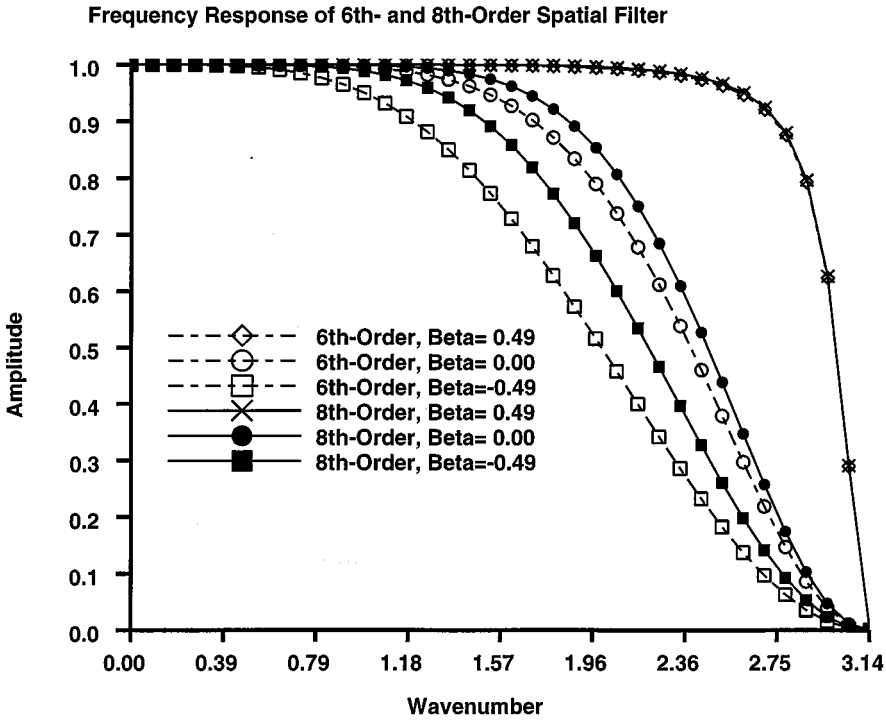

FIG. 1. Frequency response of high-order spatial filter.

also coincides with the theoretical upper limit of numerical resolution for the sixth-order compact-difference scheme, when operating on a one-dimensional model wave equation. In terms of grid-point density utilization, this value corresponds to a value of 8 points per wavelength. Similarly, the threshold of the sixth-order filter is also compatible with the fourth-order compact-difference scheme, except that the theoretical resolution limit is reduced to a value around 12 points per wavelength.

6. NUMERICAL RESULTS

All present results have been processed on the Cray C916/16256 computing system. The sparse tridiagonal matrices which arise from the spatial derivative calculation are solved by the classic Thomas algorithm [15]. The data processing rate of the compact-difference schemes is significantly reduced on a vector processor because of the recursive arithmetic operations of the matrix inversion process. The data processing rate is degraded from 610 to 307 Mflops just by including this recursive formulation. The issues of improving computational efficiency and scalability of the compact-difference schemes on multicomputers offer meaningful challenges to expand the time-domain methods from the resonance to the optical regime [3].

The presentation of numerical results is separated into three groups. The first group summarizes performance of the fourth-order (FD46) and sixth-order (FD66, FD68) compact-difference schemes applied to three-dimensional transient electromagnetic waves within a rectangular guide. The designation of FDxy stands for a x-order spatial accurate and y-order filter finite-difference scheme. The angular frequency ω of transmitted waves span

a spectrum from 3π to 6π, which corresponds to the grid-point density from 18.5 to 8.25 per wavelength. At the highest frequency, the transient wave will travel a total distance of 250 wavelenghts before data are sampled. The numerical solution is evaluated in the form of the normalized L2 norm of the deviation from the corresponding theoretical value. The main emphasis is on investigating the resolution characteristics of different high-order schemes by spectral analysis.

The second group of computations describe the radiation field of an oscillating electrical dipole. The numerical resolution of the compact-difference scheme is compared with conventional methods near the singular point of the dipole. The effectiveness of the spatial filter in controlling the time instability is also highlighted.

The third group details scattering computations of a PEC sphere for a wavenumber of 20.0. Since the sphere is assigned a diameter of unity, the parameter of the validating Mie series yields the values of 10.0 [25, 26]. The computational domain is bounded by two concentric spheres and is easily accommodated by a spherical coordinate system. The inner sphere describes the unit spherical scatterer, and the outer sphere defines the truncated farfield boundary. For this series of simulations, the truncated computational domain is consistently placed more than three wavelengths from the sphere surface.

In Fig. 2, the x-component of the magnetic flux density, B_x, of the transverse electrical wave, TE(1, 1), within a rectangular waveguide is depicted at three different frequencies. All numerical solutions are generated by either the sixth- or fourth-order compact-difference schemes on a uniformly spaced grid (25, 25, 97). The instantaneous B_x distributions along the entire length of the waveguide are accompanied by the theoretical values for validation [1]. At the lower frequency spectrum, $\omega = 3\pi$, numerical results of the entire

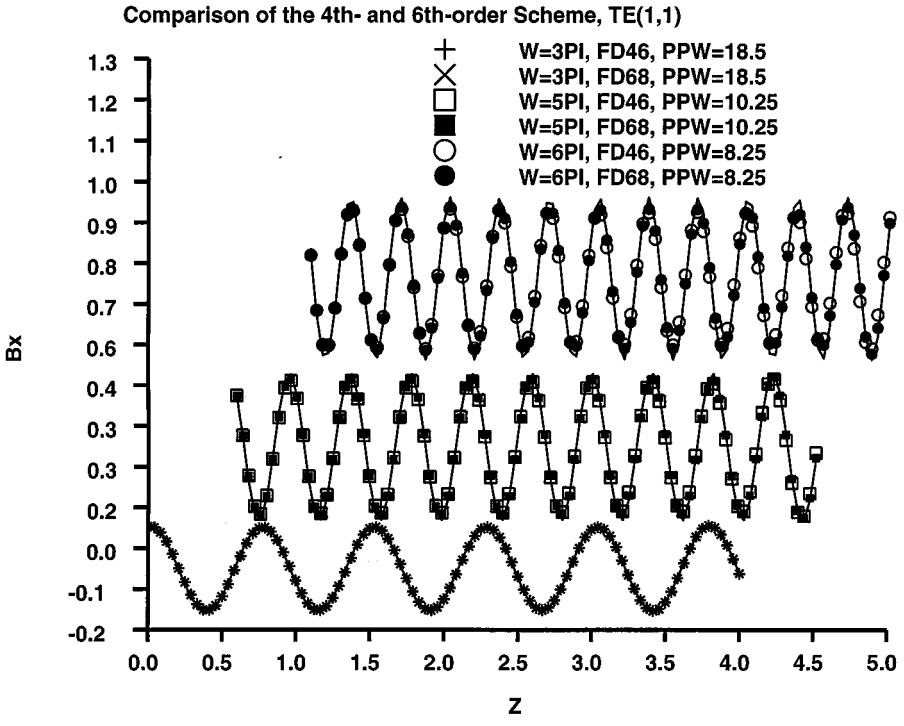

FIG. 2. Comparison of the fourth- and sixth-order compact-difference schemes.

electromagnetic field of both schemes are nearly identical. At each discretized point, the solutions are accurate, yielding the L2 norm values of $O(10^{-6})$ and $O(10^{-4})$, respectively. Similar numerical accuracy is also obtained by comparison with the theory at the higher frequency spectrum from 5π to 6π, which corresponds to a grid-point density from 10.25 to 8.25 per wavelength. From the previous work [9] and the present results, the numerical error of a second-order scheme already becomes unacceptable. At the highest frequency, with the numerical results representing the wave after propagating a distance of 23.5 wavelengths, the dispersive and dissipative errors are still confined within a magnitude of $O(10^{-4})$. Unfortunately, these errors are accumulated as the simulated wave is propagated farther along the waveguide.

An equally important observation is also made by comparing the two compact-difference schemes. The combination of the sixth-order scheme with a sixth-order and an eighth-order spatial filter (FD66 and FD68) produces essentially identical results. The FD66 or FD68 scheme has a pentadiagonal stencil structure, and a fifth-order one-sided boundary scheme is required to complete the formulation. As a result, both FD66 and FD68 schemes need additional transitional boundary schemes immediately adjacent to the boundary. On the other hand, the fourth-order scheme is a tridiagonal system, and only a fourth-order one-sided differencing approximation on the boundary is required. The numerical accuracy of FD66 and FD46 reflects correctly the relatively formal order of each formulation. However, the accuracy advantage of the sixth-order scheme over the fourth-order scheme is also marginal due to the staged boundary schemes and the spatial filters. The FD46 scheme proves to be the most robust and effective in controlling the time instability. For this reason, the fourth-order scheme is considered to be optimal for applications, and the rest of the present effort is focused on the further refinement of the FD46 scheme.

Figure 3 depicts the effectiveness and numerical behavior of the spatial filter when applied to a transient TE(1, 1) wave. The numerical result shows the instantaneous z-component of the electric displacement, D_z, at an angular frequency $\omega = 3\pi$. For the transverse electric wave, the theoretical value of the electrical field component is zero; thus the non-zero numerical results reflect the numerical error incurred by FD46 on a (25, 25, 97) grid system. The parameter β assigned the value of 0.5 corresponds to the situation that the numerical results are not filtered. The even–odd decoupling phenomenon near the waveguide entrance is clearly exhibited. As expected, the perturbation introduced by the boundary scheme is the major source of the time instability. Over a range of the filter parameter β from 0.25 to -0.25, the spurious and parasitic high-frequency components are effectively removed. In addition, the numerical results seem relatively insensitive to the specific value of the filter parameter β. In other words, the filter effectively modifies the amplitude of the unresolvable and non-physical high-frequency Fourier components of numerical solutions. At this frequency, only a time lapse of 5 periods is needed for the transient wave to traverse the entire length of the waveguide. However, the accurate and stable numerical result is sampled after the calculation is sustained for a duration of 20 periods.

The substantiation of the above observation that only the unsupportable and non-physical Fourier components are eliminated by the spatial filter is given in Fig. 4. In this figure, the coefficients of Fourier components of the calculated y-components of the magnetic flux density at $\omega = 3\pi$ and $\omega = 6\pi$ are given. The spectral comparison is developed by a 47-term Fourier series. Similar results also have been obtained for all other field components of the TE(1, 1) wave. In wave space, any Fourier component having a wavenumber greater

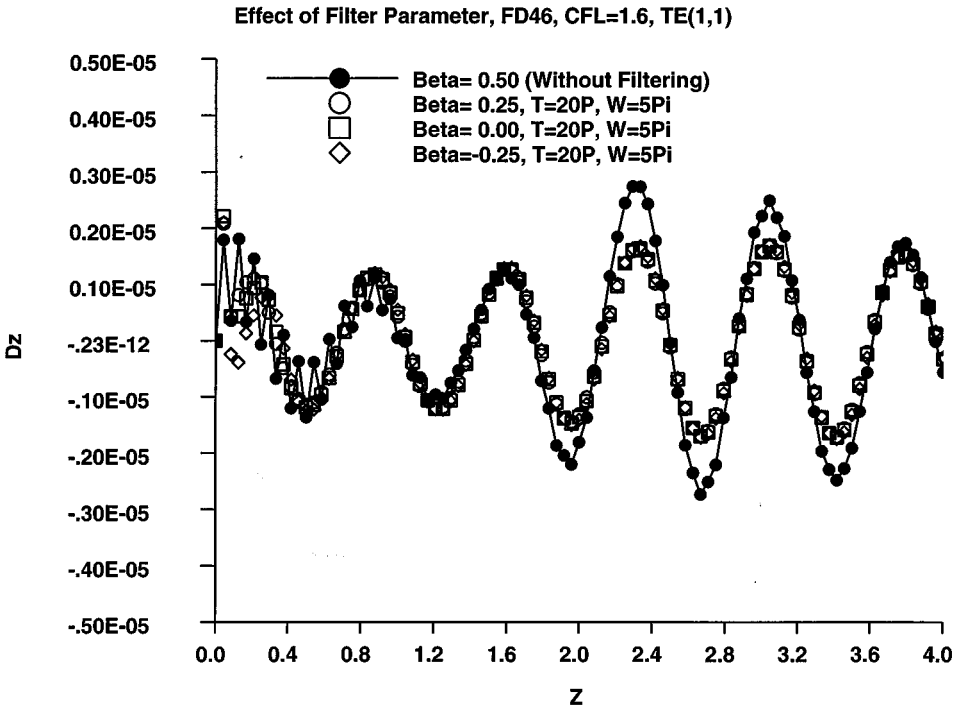

FIG. 3. Effect of filter parameter to waveguide simulations.

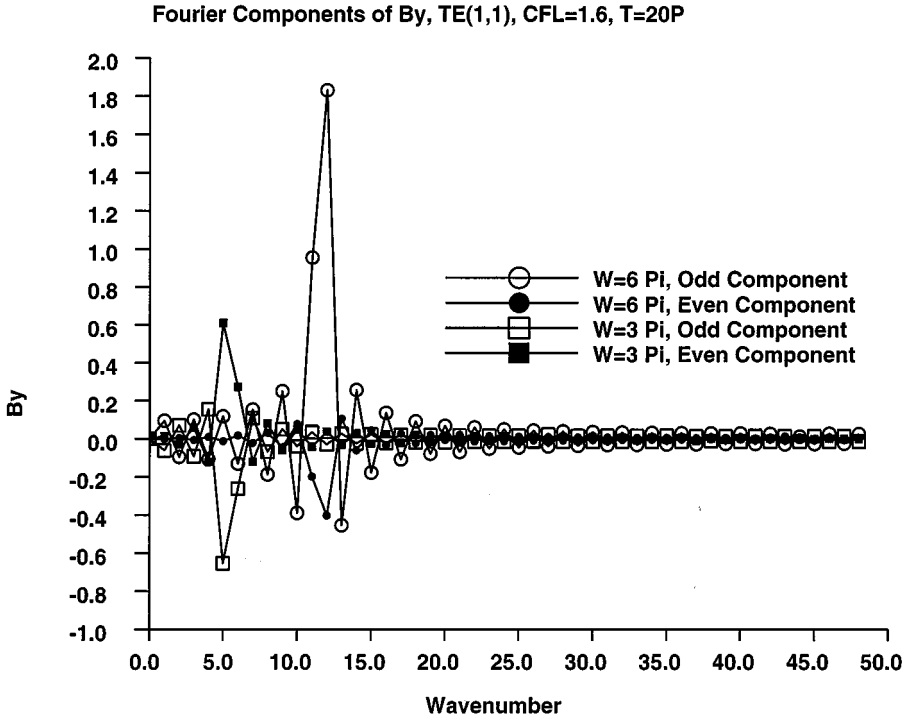

FIG. 4. Spectral analysis of waveguide numerical solution.

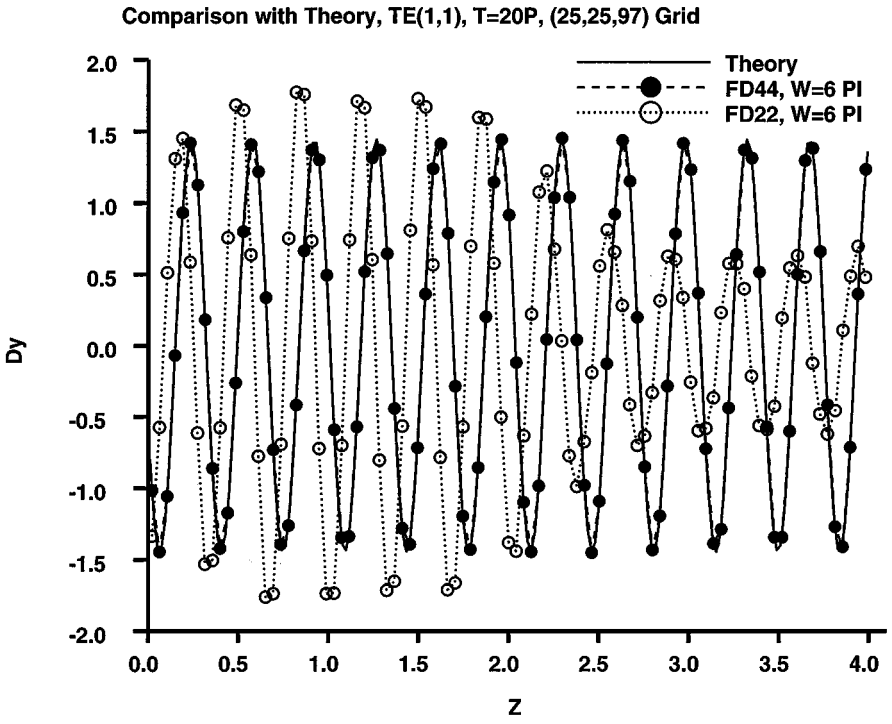

FIG. 5. Error pattern of schemes in waveguide simulations.

than 16 is not supportable by the (25, 25, 97) gird system. The spectral results reveal that the amplitudes of the upper range of the spurious high frequency are favorably modified.

A specific comparison to illustrate the superior numerical resolution of the compact-difference scheme over the conventional second-order midpoint leapfrog method is presented in Fig. 5. Numerical results of the y-component electric displacement D_y, at an angular frequency of 6π, are presented together with the theoretical result [1]. Under the extremely sparse grid-point density condition, 8.25 points per wavelength, the most widely used second-order scheme [2, 3] can no longer generate a credible result. For a relatively short waveguide calculation of 20 wavelengths, the dissipative error of the FD46 scheme is less than $O(10^{-4})$ and the dispersive error is equally negligible.

Finally, the most critical issue of controlling the time instability of a compact-difference scheme is depicted by sustained transient calculations for a TE(1, 1) wave. A longer waveguide dimension than was used in the previous calculations is described by a (25, 25, 399) grid system. Numerical results for four angular frequencies 3π, 4π, 5π, and 6π are generated. The corresponding waveguide dimensions at different frequencies in terms of wavelength are 21.6, 30.1, 38.9, and 48.4, respectively. At a CFL $= 1.4$, the calculation of the highest frequency is sustained for a duration to propagate the wave a distance of 250 wavelengths. For all calculations, the filter parameter, β, is assigned a value of 0.475, close to the lower parametric limit. Only three higher frequency x-components of the electric displacement are accompanied by theoretical values to illustrate these results briefly. In Fig. 6, the result near the exit plane of the waveguide is presented to highlight a detailed comparison with the theory. At lower frequencies, the maximum discrepancy from the theory is still within the tolerance of an L2 norm value of $O(10^{-4})$ both in dissipation and

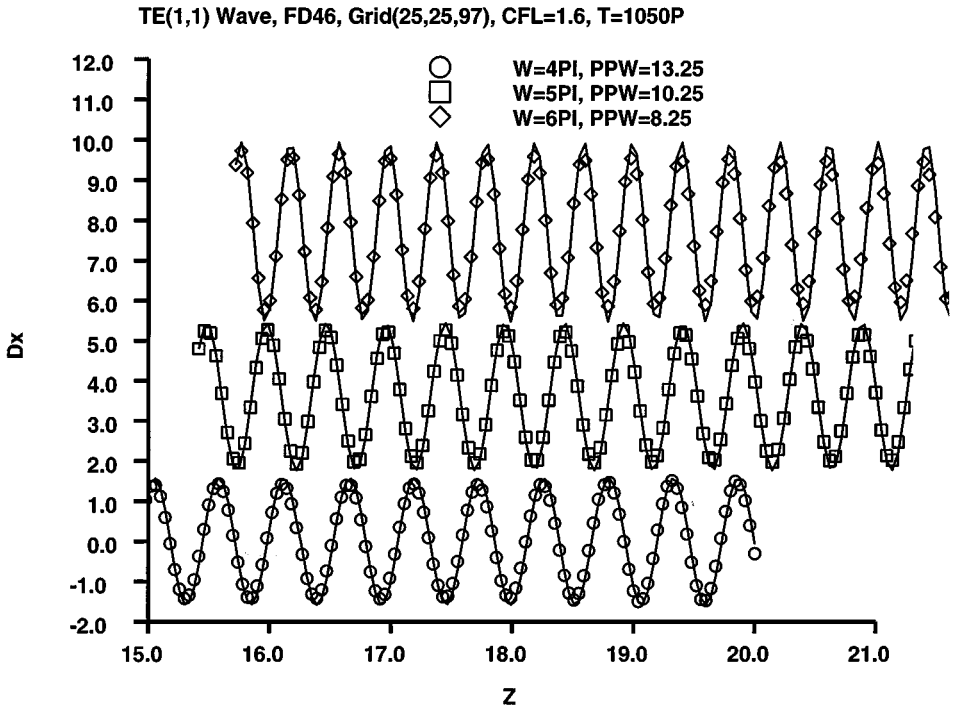

FIG. 6. Compact-difference solutions of TE(1, 1) waves.

in dispersion. This quantification holds true for $\omega = 3\pi$, 4π, and 5π, but with increasing accuracy degradation as the frequency is increased. For the highest frequency examined, $\omega = 6\pi$, the numerical errors become excessive. The dissipative error has exceeded 5% with respect to the theoretical result; the relative phase error also has a magnitude of more than 6%.

The observed errors are accumulated as time or the distance of wave propagation progresses in the calculation. However, the degradation in numerical results is far less measurable as long as the grid-point density is within a reasonable wavenumber range for the compact-difference scheme. At the extremely sparse grid density condition, a higher order spatial filter also has a limited range of effectiveness. In this wavenumber region, the physical and spurious components may not be separable on the supporting grid system.

Unfortunately, a perfectly matched-layer boundary condition at the exit plane of the waveguide [25–27] was not accomplished in time for inclusion in the study of critical boundary effects. Based on the present numerical results, one concludes that the high-order compact-difference schemes can generate a higher resolution simulation of transient electromagnetic waves in a waveguide than the conventional finite-difference methods. The high-frequency filters can suppress but are unable to eliminate all spurious high-frequency Fourier components of the numerical solution during sustained periods of computation.

In Fig. 7, the superior numerical resolution of the compact-difference scheme is demonstrated near the singular point by an oscillating electric dipole simulation [1]. The entire electromagnetic field is generated by an alternating current element at an angular frequency of $\omega = 2\pi$. The x-component of the magnetic flux density, B_x, computed by the compact-difference scheme (FD46), a temporally fourth-order and spatially third-order finite-volume scheme (FV43) [23], and a second-order finite-difference scheme (FD22) [28] is presented together with theoretical results. The electric and magnetic fields of the oscillating dipole

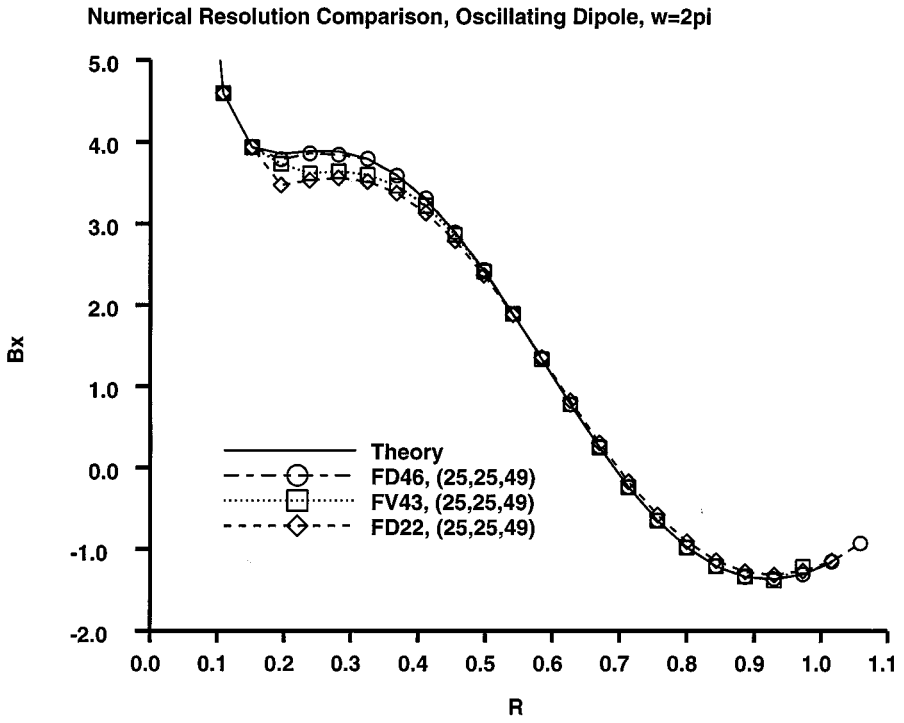

FIG. 7. Numerical resolution comparison for oscillating dipole computations.

have an $O(1/r^3)$ and $O(1/r^2)$ singular behavior at the pole, respectively, thus inducing a rapidly varying field in time and space. All numerical results are processed on a (25, 25, 49) grid system for the radial range $0 < r < 1.1$. The ability of the fourth-order compact difference scheme to resolve the steep gradient region better than conventional methods is easily detectable. Both conventional methods incur a local error around 10%, and the error of the popular second-order scheme, FD22, even propagates across the entire computational domain.

The critical importance of spatial filter performance to suppress the time instability and to maintain numerical accuracy is exhibited in Figs. 8 and 9. The quantification of numerical error for the oscillating electric dipole is represented by the L2 norm of the z-component of the magnetic flux density, L2 norm (B_z). For the radiation problem, the theoretical value of this field component is zero. Therefore, a non-zero value is indicative of the magnitude of numerical error. In Fig. 8, the numerical data supported by a fourth-order spatial filter is collected over a duration of 8 periods. A total of five calculations are performed using different parametric values of the filter. As a reference of comparison, the time-dependent calculation without the use of spatial filter diverged at the time elapse of 3.4 periods.

In Fig. 8, the calculation using the lower value of the filter parameter, $\beta = 0.49$, defines the theoretical limit of numerical accuracy on a (25, 25, 97) grid. The numerical results are actually improved by using the values of the parameter in the allowable range, $-0.5 < \beta < 0.5$. More importantly, all computations are sustained over 20 periods. Similar numerical behavior is also observed for computations using the six-order filter.

In Fig. 9, the numerical result of the sixth-order filter is depicted for the same parametric value as before. The main difference in the solutions is that numerical results using the

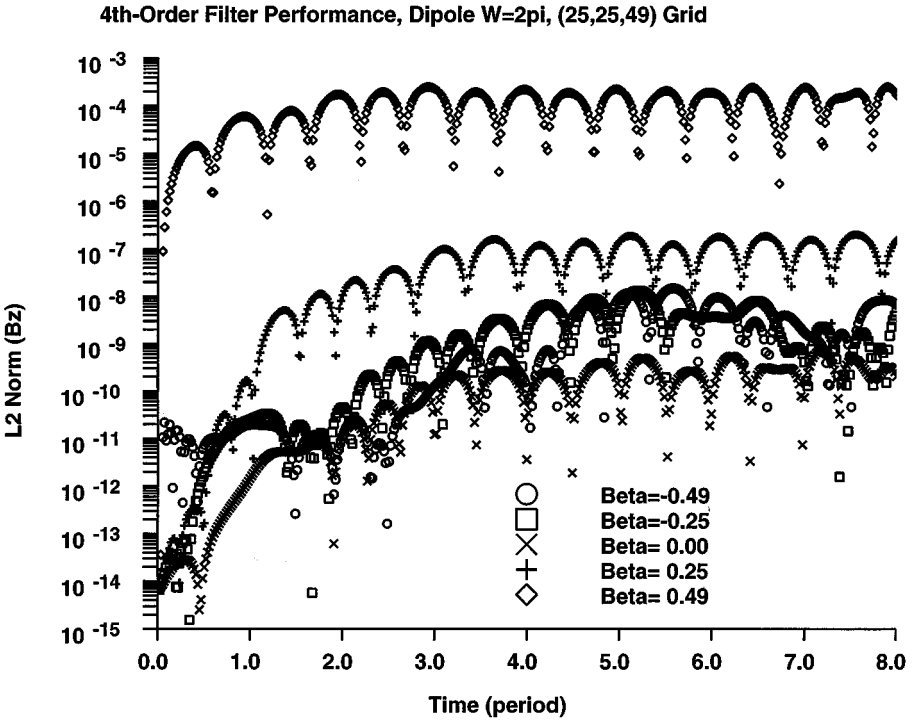

FIG. 8. Fourth-order filter performance on dipole calculations.

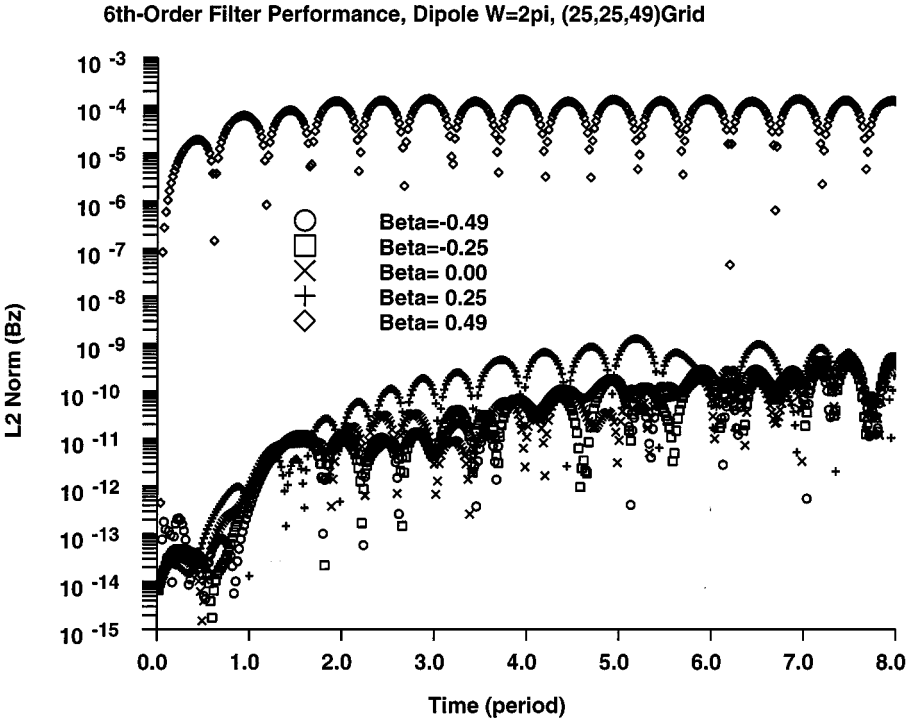

FIG. 9. Sixth-order filter performance on dipole calculations.

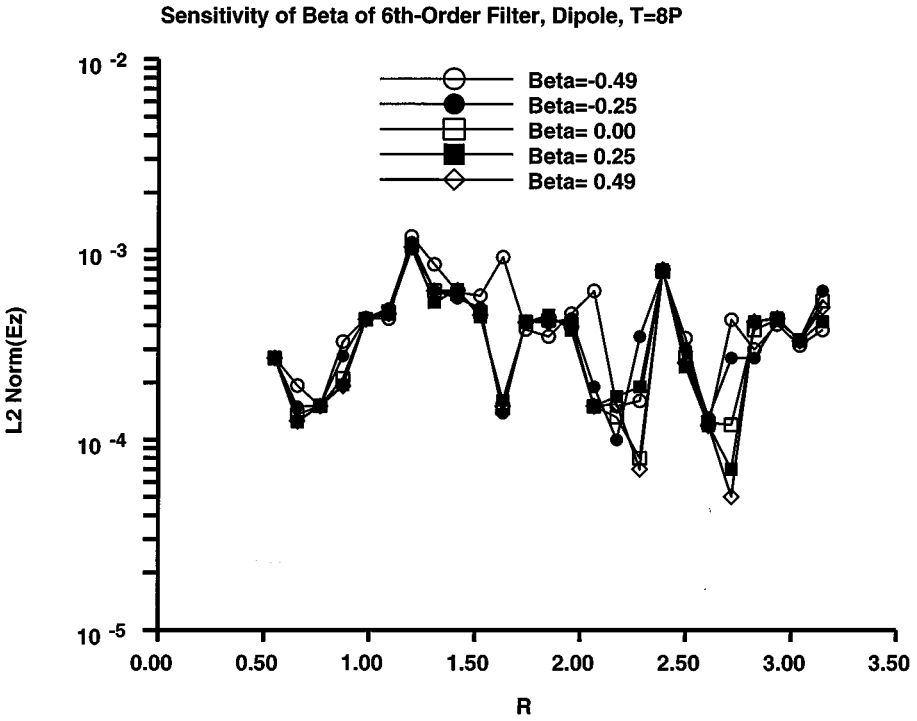

FIG. 10. Sensitivity of filter parameter to dipole calculations.

sixth-order scheme are clustered tighter than those using the fourth-order filter, and the numerical errors also have a lower magnitude. This particular feature is understandable if one recalls that the sixth-order filter has a narrower frequency response range than the fourth-order filter. Numerical accuracy has been maintained up to the duration of 20 periods, which is five times the requirement for the radiation calculation. From this result, it seems that a higher order filter should be preferred. However, the higher order filter also has a wider stencil dimension, resulting in a more restricted applicable domain near boundaries. In the case of a strong interaction between the boundary scheme and the spatial filter, the choice of filter is problem specific.

A group of computations by the FD46 scheme using the same range of values of β parameter are given in Fig. 10. On a coarser (25, 25, 49) grid, the calculated L2 norm error of the z-component of electric displacements, E_z, is presented. The numerical results agree well with the theory, and the discrepancy among all numerical results is confined within a scattering band from $O(10^{-3})$ to $O(10^{-4})$. For this series of calculations, the solutions reveal a relative insensitivity to the choice of filter parameter value. The above comparison essentially completes the presentation of the spatial filter performance.

In Fig. 11, the numerical resolution limit of the fourth-order compact difference scheme is assessed for the unsteady radiation simulation. Only two numerical results of the x-component electric displacement at a grid-point density of 10 and 8 points per wavelength are given. For the denser grid-point density computation, the numerical result processed on a (51, 51, 97) grid system attains uniformly excellent agreement with the theory. The maximum discrepancy of numerical result from the theoretical value is less than $O(10^{-4})$. As the grid-point density is reduced from 10 to 8, significant errors start to appear in the

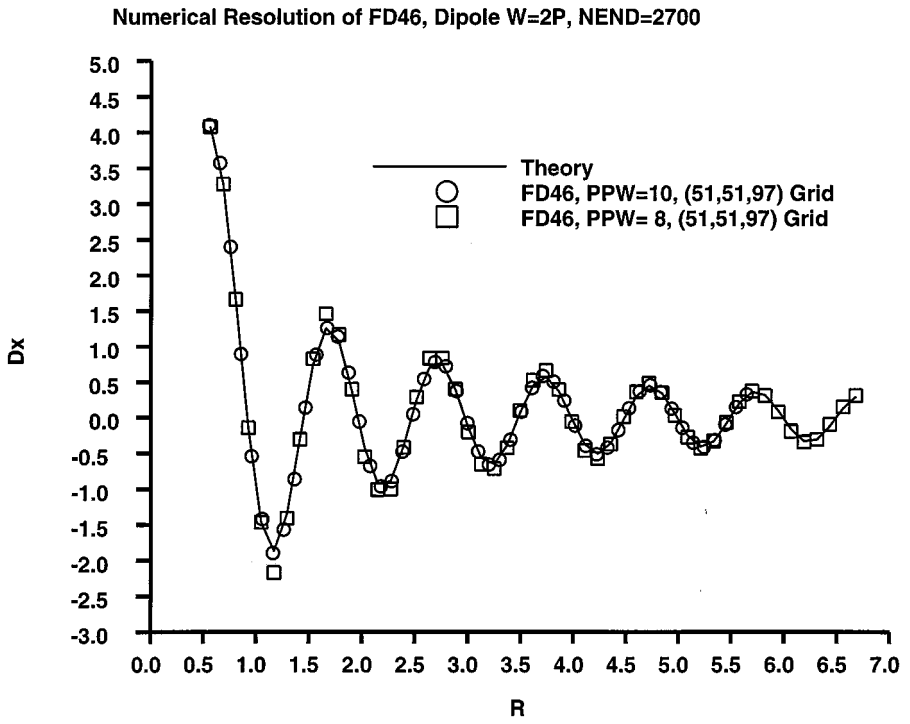

FIG. 11. Numerical resolution of FD46 for dipole calculations.

high-gradient region near the polar singularity. This observation is consistent with analyses of the transverse electrical wave propagating in the waveguide.

The effectiveness of suppressing spurious high-frequency components by using a spatial filter for the radiation simulation is illustrated in Fig. 12. The calculated y-component magnetic flux densities from two different calculations are accompanied by the theoretical result. For this simulation at $\omega = 2\pi$, the non-physical result of an unfiltered calculation will emerge shortly after a time lapse of 3.4 periods. Once the spatial filter is actuated, accurate numerical results can be obtained after 20 periods of temporal evolution. However, only an accurate result after 10 periods of evolution is needed for the time-dependent simulation. This duration of computation is four times the value needed for an electromagnetic wave to propagate from the dipole center to the outer edge of the computational domain. The difference between the solution generated at 5 periods (1350 time steps at CFL $= 1.42$) and 10 periods (2700 time steps) is well within the expected accuracy measured by the L2 norm of B_y, $O(10^{-4})$.

In Fig. 13, the spectral analysis of the aforementioned numerical results in the radial direction is presented. The amplitude of the Fourier coefficients is plotted against the entire range of wavenumbers. A 25-term Fourier series is used to approximate the numerical solutions, including the full complement of even and odd components. Since the electromagnetic wave is modulated as it propagates outward, not all high-frequency components are diminished. The important issue is that all the corresponding Fourier components are nearly identical for the two solutions that are sampled at different time intervals. This additional evidence further confirms that the time instability of the oscillating electric dipole is suppressed up to at least 10 periods.

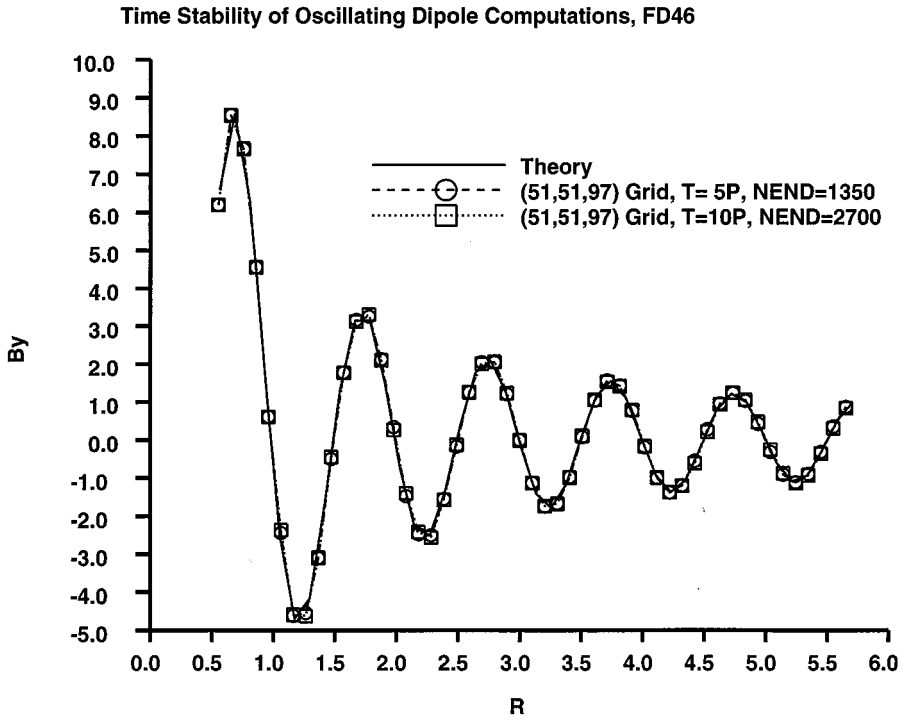

FIG. 12. Time stability of oscillating dipole calculations.

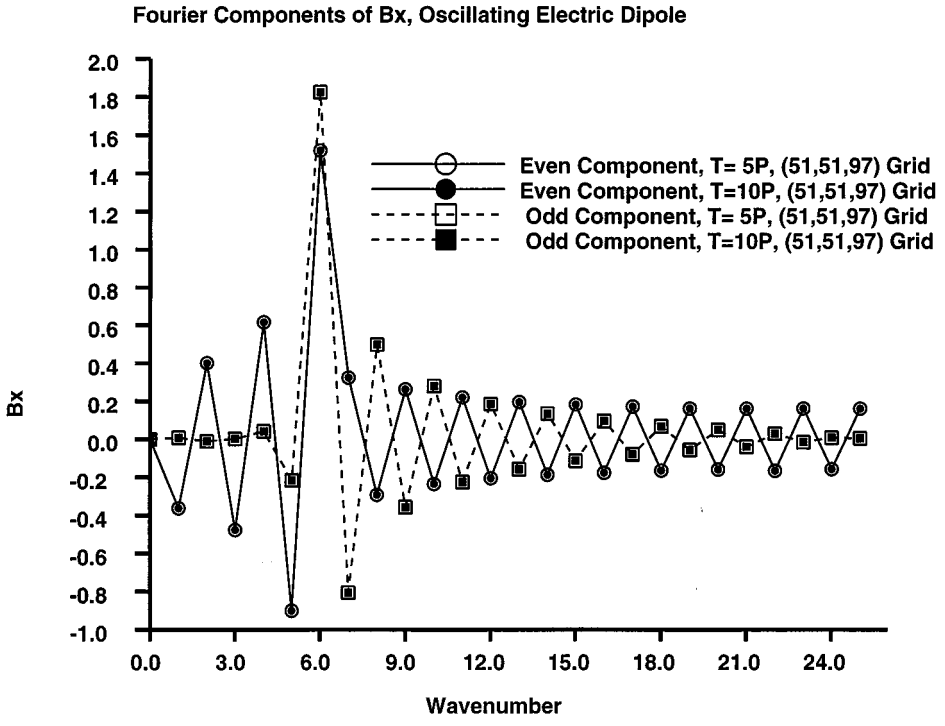

FIG. 13. Spectral analysis of dipole calculations.

The last group of presentations consider the radar cross-section calculations for a PEC sphere. For a unit sphere illuminated by a linearly polarized harmonic field with wavenumber 20.0, the κa (a is the radius of the sphere) parameter of the Mie series has the value of 10.0. For the (73, 61, 96) grid, the grid spacing in the radial (r) direction is stretched, while the azimuthal and the circumferential angular displacements ($\Delta\theta$ and $\Delta\phi$) remain at constant values. The grid-point density is most sparse at the farfield in the circumferential orientation, 9.6 points per wavelength.

In the process of radar cross-section calculations, all electromagnetic components, E and H, are first transformed in the frequency space by a Fourier transform. Then the farfield asymptotes for the RCS computation are obtained by a nearfield to farfield transformation [29, 30]

$$\begin{aligned}\sigma(\theta,\phi) &= (i\kappa/4\pi)\int\int_s [\sqrt{\mu/\epsilon}(\vec{n}\times H) - (\vec{n}\times E)\times\vec{r} - (\vec{n}\cdot E)\vec{r}]e^{-i\kappa r\cdot\hat{r}}\,dS \\ \sigma(\theta,\phi) &= -(i\kappa/4\pi)\int\int_s [\sqrt{\epsilon/\mu}(\vec{n}\times E) + (\vec{n}\times H)\times\vec{r} + (\vec{n}\cdot H)\vec{r}]e^{-i\kappa r\cdot\hat{r}}\,dS,\end{aligned} \tag{20}$$

where $\vec{n}$ and $\vec{r}$ denote the surface outward normal of the scatterer and the unit vector of the observation direction.

Figure 14 depicts the normalized bi-static RCSs in horizontal polarization, $\sigma(\theta, 0.0)$, obtained using the Fourth-order compact-difference (FD46) and the Mie series [30]. The solution of a second-order scheme is also included for the sole purpose of assessing computational efficiency. The present calculation attains a reasonable agreement with the theoretical result. The maximum discrepancy from the Mie series is in the back scattering and the transition zone between the illuminated and shadow regions with a magnitude of 2 dbs. A

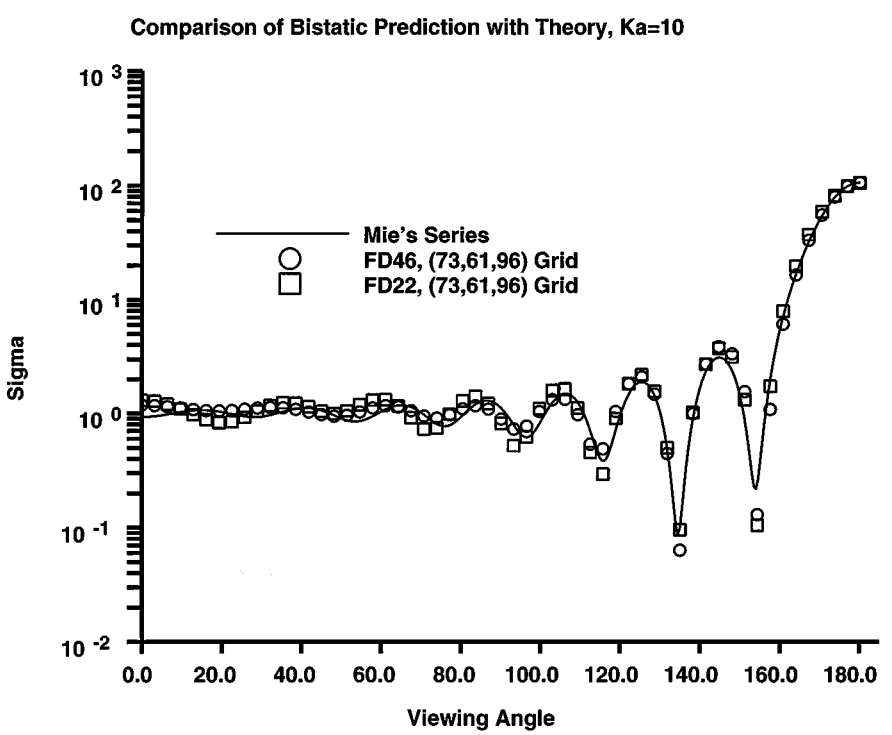

FIG. 14. Comparison of bistatic RCS, $\sigma(\theta, 00.0)$, $\kappa a = 10$.

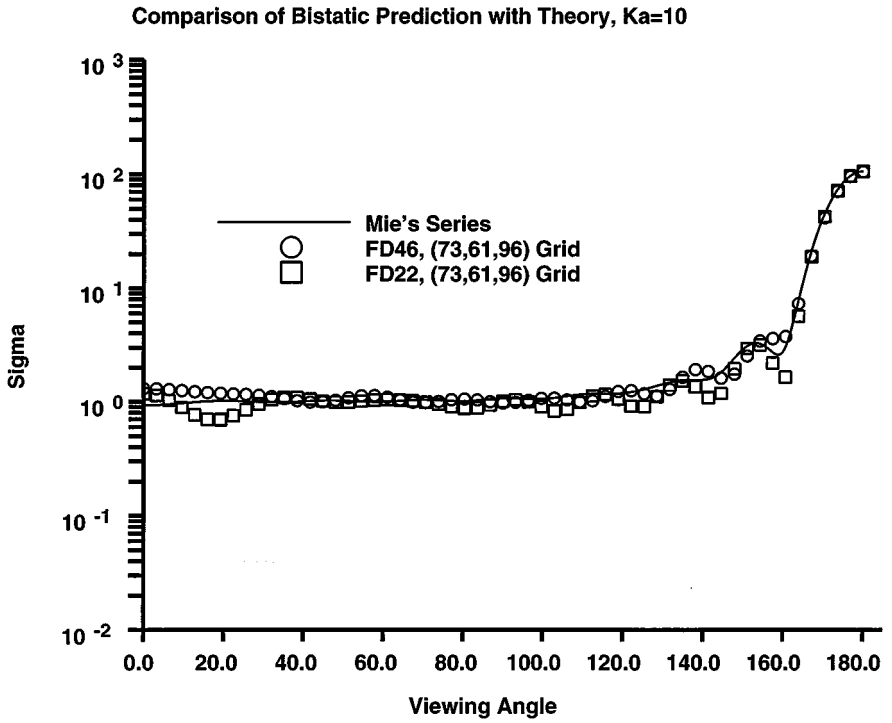

FIG. 15. Comparison of bistatic RCS, $\sigma(\theta, 90.0)$, $\kappa a = 10$.

major detriment for a better accuracy is directly attributable to the farfield boundary condition. This numerical boundary condition of the compact-difference scheme essentially dictates the solution accuracy. For the FD46 calculation, the farfield boundary is placed further away by geometric series stretching in radial direction than the FD22 calculation, using the same number of grid points. The result by the FD46 scheme exhibits a slight improvement over the results of the FD22 scheme using the same number of grid points.

The CFL number of the FD46 scheme has nearly a three times greater allowable value than the FD22 (1.42 vs 0.5). The data propagation within the computational domain is also accelerated by the implicit derivative evaluation. The short transition from the initial condition is a direct consequence of a greater domain of dependence of the implicit calculations. The required transition period before electromagnetic field data can be sampled is reduced from 4 periods to 1 [23, 24]. The potential CPU time saved is a factor of 4 or more; however, only a reduction of 3.5 times is realized. The lost computing efficiency is incurred by recursive matrix inversion calculations, which will be addressed in the future.

The normalized bi-static RCS in vertical polarization, $\sigma(\theta, 90.0)$, for $\kappa a = 10.0$ is presented in Fig. 15. The numerical solution features from FD46 and FD22 are similar. The maximum numerical error is again around 2 dbs and occurs in the same regions as the RCS results of the horizontal polarization. Unfortunately, the accuracy degradation by the stretched coordinate system to the present compact-difference is uncertain.

7. CONCLUDING REMARKS

Sixth- and fourth-order compact-difference schemes with high-order spatial filters have been successfully developed. The fourth-order scheme is considered to be optimal at the

present time. Significant improvements of numerical resolution have been illustrated for electromagnetic wave propagation in a waveguide and a radiation problem.

The spatial filter has been demonstrated to suppress the spurious and parasitic high-frequency components for the numerical schemes examined. However, the time instability of compact-difference schemes is not completely eliminated in the present investigation.

The use of compact-difference approximations to solve the three-dimensional, time-dependent Maxwell equations shows promising potential in extending the frequency spectra for practical applications.

ACKNOWLEDGMENTS

The author deeply appreciates the helpful review by Drs. D. V. Gaitonde and D. P. Rizzetta. Sponsorship by Dr. A. Nachman is also gratefully acknowledged. This work was supported in part by a grant of HPC time from the Department of Defense HPC Shared Resource Centers at WPAFB.

REFERENCES

1. J. A. Stratton, *Electromagnetic Theory* (McGraw–Hill, New York, 1941).
2. A. Taflove, *Advances in Computational Electromagnetics: The Finite-Difference Time Domain Method* (Artech House, Norwood, MA, 1998).
3. J. S. Shang, Challenges for computational electromagnetics in the time domain, in *1997 IEEE International Symposium on Antennas and Propagation, Montreal, Canada, July 13–17, 1997*, Vol. 1, p. 94.
4. S. K. Lele, Compact finite difference schemes with spectral-like resolution, *J. Comput. Phys.* **103**, 16 (1992).
5. M. K. Carpenter, D. Gottlieb, and S. Abarbanel, Time-stable boundary conditions for finite-difference schemes solving hyperbolic systems: Methodology and application to high-order compact schemes, *J. Comput. Phys.* **111**, 220 (1994).
6. C. K. W. Tam and J. C. Weber, Dispersion-relation-preserving finite difference schemes for computational acoustics, *J. Comput. Phys.* **107**, 262 (1993).
7. L. Collatz, *The Numerical Treatment of Differential Equations* (Springer-Verlag, New York, 1966), p. 538.
8. Y. Adam, Highly accurate compact implicit methods and boundary conditions, *J. Comput. Phys.* **24**, 10 (1977).
9. J. S. Shang and D. V. Gaitonde, On high resolution schemes for time-domain maxwell equations (AIAA 96-0832), in *34th AIAA Aerospace Science Meeting, Reno, NV, Jan. 15–18, 1996.*
10. J. L. Young, D. Gaitonde, and J. S. Shang, Towards the construction of a fourth-order difference scheme for transient EM wave simulation: Staggered grid approach, *IEEE Trans. Antennas Propagation* **45**, 1573 (1997).
11. D. V. Gaitonde and J. S. Shang, High-order finite-volume schemes in wave propagation phenomena (AIAA 96-2335), in *27th Plasmadynamics and Laser Conference, New Orleans, LA, June 17–20, 1996.*
12. D. V. Gaitonde and J. S. Shang, Practical aspects of high-order accurate finite-volume scheme for electromagnetics (AIAA 97-0363), in *35th Aerospace Science Meeting, Reno, NV, Jan. 6–10, 1997.*
13. D. V. Gaitonde and J. S. Shang, Optimized compact-difference-based finite-volume schemes for linear wave phenomena, *J. Comput Phys.* **138**, 617 (1997).
14. M. R. Visbal and D. V. Gaitonde, High-order accurate methods for unsteady vortical flows on curvilinear meshes (AIAA 98-0131), in *36th Aerospace Science Meeting, Jan. 12–15, 1998.*
15. D. A. Anderson, J. C. Tannehill, and R. H. Pletcher, *Computational Fluid Mechanics and Heat Transfer* (McGraw–Hill, New York, 1984).
16. B. Gustafsson, H.-O. Kreiss, and A. Sundstrom, Stability theory of difference approximations for mixed initial boundary value problem, II, *Math. Comp.* **26**, 649 (1972).
17. B. Gustafsson, The convergence rate for difference approximations to mixed initial boundary value problems, *Math. Comp.* **29**, 396 (1975).
18. B. Gustafsson and P. Olsson, Fourth-order difference methods for hyperbolic IBVPs, *J. Comput. Phys.* **117**, 300 (1995).

19. M. K. Carpenter, D. Gottlieb, and S. Abarbanel, The stability of numerical boundary treatments for compact high-order finite-difference schemes, *J. Comput. Phys.* **108**, 272 (1993).
20. R. Vichnevetsky, *Numerical Filtering for Partial Differential Equations*, Numerical Applications Memorandum 156, Nov. 1974.
21. R. Vichnevetsky and J. B. Bowles, *Fourier Analysis of Numerical Approximations of Hyperbolic Equations*, SIAM Studies in Applied Mathematics (SIAM, Philadelphia, 1982).
22. B. Carnahan, H. A. Luther, and J. O. Wilkes, *Applied Numerical Methods* (Wiley, New York, 1969), p. 361.
23. J. S. Shang and D. Gaitonde, Characteristic-based, time-dependent Maxwell equations solvers on a general curvilinear frame, *AIAA J.* **33**, 491 (1995).
24. J. S. Shang and R. M. Fithen, A comparative study of characteristic-based algorithms for the Maxwell equations, *J. Comput. Phys.* **125**, 378 (1966).
25. J. A. Berenger, A perfectly matched layer for the absorption of electromagnetic waves, *J. Comput. Phys.* **114**, 185 (1994).
26. W. C. Chew and J. M. Jin, Perfectly matched layers in the discretized space: An analysis and optimization, *Electromagn.* **16**, 325 (1996).
27. P. G. Petropoulos, L. Zhao, and A. C. Cangellaris, A reflectionless sponge layer absorbing boundary condition for the solution of Maxwell's equations with high-order staggered finite difference schemes, *J. Comput. Phys.* **139**, 184 (1998).
28. J. S. Shang, A fractional-step method for the time domain Maxwell equations, *J. Comput. Phys.* **118**, 109 (1995).
29. J. W. Crispin and K. M. Seigel, Eds., *Methods of Radar Cross-Section Analysis* (Academic Press, New York, 1968), p. 3.
30. J. J. Bowman, T. B. A. Senior, and P. L. E. Uslenghi, Eds., *Electromagnetic and Acoustic Scattering by Simple Shapes* (Hemisphere, New York, 1987), p. 353.